The Astrophysical Journal, 928:147 (12pp), 2022 April 1 https://doi.org/10.3847/1538-4357/ac54b8

Simulating the Space Weather in the AU Mic System: Stellar Winds and Extreme Coronal Mass Ejections

Julián D. Alvarado-Gómez[1,8], Ofer Cohen[2], Jeremy J. Drake[3], Federico Fraschetti[3,4], Katja Poppenhaeger[1,5], Cecilia Garraffo[3], Judy Chebly[1,5], Ekaterina Ilin[1,5], Laura Harbach[6], and Oleg Kochukhov[7]
[1] Leibniz Institute for Astrophysics Potsdam, An der Sternwarte 16, D-14482 Potsdam, Germany; julian.alvarado-gomez@aip.de
[2] University of Massachusetts at Lowell, Department of Physics & Applied Physics, 600 Suffolk Street, Lowell, MA 01854, USA
[3] Center for Astrophysics | Harvard & Smithsonian, 60 Garden Street, Cambridge, MA 02138, USA
[4] Department of Planetary Sciences-Lunar and Planetary Laboratory, University of Arizona, Tucson, AZ 85721, USA
[5] University of Potsdam, Institute for Physics and Astronomy, Karl-Liebknecht-Str. 24/25, D-14476 Potsdam, Germany
[6] Imperial College London, Astrophysics Group, Department of Physics, Prince Consort Road, London, SW7 2AZ, UK
[7] Department of Physics and Astronomy, Uppsala University, Box 516, SE-75120 Uppsala, Sweden

Received 2021 November 23; revised 2022 January 26; accepted 2022 February 14; published 2022 April 4

Abstract

Two close-in planets have been recently found around the M-dwarf flare star AU Microscopii (AU Mic). These Neptune-sized planets (AU Mic b and c) seem to be located very close to the so-called "evaporation valley" in the exoplanet population, making this system an important target for studying atmospheric loss on exoplanets. This process, while mainly driven by high-energy stellar radiation, will be strongly mediated by the space environment surrounding the planets. Here we present an investigation of this last area, performing 3D numerical modeling of the quiescent stellar wind from AU Mic, as well as time-dependent simulations describing the evolution of a highly energetic coronal mass ejection (CME) event in this system. Observational constraints on the stellar magnetic field and properties of the eruption are incorporated in our models. We carry out qualitative and quantitative characterizations of the stellar wind, the emerging CMEs, as well as the expected steady and transient conditions along the orbit of both exoplanets. Our results predict extreme space weather for AU Mic and its planets. This includes sub-Alfvénic regions for the large majority of the exoplanet orbits, very high dynamic and magnetic pressure values in quiescence (varying within 10^2–10^5 times the dynamic pressure experienced by Earth), and an even harsher environment during the passage of any escaping CME associated with the frequent flaring observed in AU Mic. These space weather conditions alone pose an immense challenge for the survival of exoplanetary atmospheres (if any) in this system.

Unified Astronomy Thesaurus concepts: Stellar magnetic fields (1610); Stellar coronal mass ejections (1881); Stellar winds (1636); Space weather (2037); Exoplanets (498); M stars (985); Red dwarf flare stars (1367); Magnetohydrodynamical simulations (1966); Star-planet interactions (2177); Plasma astrophysics (1261); High energy astrophysics (739)

Supporting material: animations

1. Introduction

AU Microscopii (AU Mic) is the 10th brightest M dwarf in the sky ($V_{\mathrm{mag}} \simeq 8.81$; Lépine & Gaidos 2011) and located at a distance of ∼9.72 pc from the Sun (Gaia Collaboration et al. 2018). It is a young (22 Myr) M1V star with a mass of $M_\star \simeq 0.50\,M_\odot$ and a radius of $R_\star \simeq 0.75\,R_\odot$ (Plavchan et al. 2020 and references therein). The star is known to harbor a ∼175 au wide (from 35 to 210 au in stellocentric distance; Kalas et al. 2004; Strubbe & Chiang 2006) edge-on debris disk, characterized by clumpy outflows evolving on timescales of months to a few years (Boccaletti et al. 2015, 2018; Grady et al. 2020).

Reflecting its young age, AU Mic rotates relatively fast ($P_{\mathrm{rot}} \simeq 4.85$ days; Kiraga 2012), displaying one of the brightest X-ray coronae in the solar neighborhood ($L_X = 5.5 \times 10^{29}$ erg s^{-1}; Hünsch et al. 1999). Significant flare activity on AU Mic has been reported from multiwavelength observations (e.g., Redfield et al. 2002; Magee et al. 2003; Mitra-Kraev et al. 2005; MacGregor et al. 2020; Martioli et al. 2021), including an energetic candidate-flare coronal mass ejection (CME) event (Cully et al. 1994; Katsova et al. 1999). Long-term photometric and spectroscopic monitoring provides evidence of a possible ∼5 yr chromospheric activity cycle in the star (Ibañez Bustos et al. 2019).

Plavchan et al. (2020) discovered a Neptune-sized planet (AU Mic b) in an ∼8.5 day period orbit and proposed a second candidate planet (AU Mic c) farther out in the system. With the aid of additional observations, Martioli et al. (2021) refined the fundamental parameters of AU Mic b ($R_b = 1.05 \pm 0.04\,R_{\mathrm{Nep}}$, $M_b = 1.00 \pm 0.27\,M_{\mathrm{Nep}}$, $a_b = 19.1 \pm 0.3\,R_\star$) and confirmed the presence of AU Mic c ($R_c = 0.84 \pm 0.04\,R_{\mathrm{Nep}}$, $0.13 < M_c\,[M_{\mathrm{Nep}}] < 1.46$) placing it in an ∼18.86 day period orbit ($a_c = 29.0 \pm 3.0\,R_\star$).

The planets of the AU Mic system appear to be located above the so-called "radius gap" in the exoplanet population (i.e., a dearth of planets with radii close to 1.5–2.0 $R_\oplus \simeq$ 0.4–0.5 R_{Nep}; Fulton et al. 2017). This feature, also known as the "evaporation valley," was predicted to be the result of atmospheric photoevaporation due to high-energy radiation (EUV, X-ray) from the host star (Owen & Wu 2013, 2017).

---

[8] Karl Schwarzschild Fellow | @AstroRaikoh

The primordial extended atmospheres of young exoplanets would make them appear larger compared to planets whose atmospheric layers would have already been removed, creating this bimodal distribution in planet size. Close-in orbits, relatively low exoplanet masses, and elevated coronal emission are expected to facilitate this process (see Owen 2019). This makes AU Mic a key object in the study of atmospheric loss, particularly as a potentially observable example of young exoplanets entering and moving across the evaporation valley, as well as an archetype for understating how environmental conditions determine the evolution of planetary systems.

While important, high-energy photon radiation is not the only aspect influencing the evolution of exoplanetary atmospheres. Planets around late-type stars orbit within a magnetized and highly ionized plasma environment. These conditions are created by the magnetic field of the host star and are subject to stochastic and secular variations driven by the unceasing fluctuations of stellar magnetic activity (see Drake et al. 2019). Known as "space weather," the interplanetary plasma conditions have a palpable effect on planets, including magnetospheric compression due to stellar wind dynamic and magnetic pressures (e.g., Vidotto et al. 2015; Garraffo et al. 2016; Alvarado-Gómez et al. 2019b), the induction of currents and subsequent Joule heating of exospheres (e.g., Cohen et al. 2018, 2020; Alvarado-Gómez et al. 2020a), and the erosion of planetary atmospheres via a range of different thermal and nonthermal processes (see Gronoff et al. 2020 for a recent review).

In this context, this study presents numerical simulations of the steady stellar wind from AU Mic, as well as the expected environment generated by an energetic CME event. These results are used to evaluate the quiescent and transient space weather experimented by planets AU Mic b and AU Mic c. Our state-of-the-art models employ observed properties of the surface magnetic field of AU Mic as boundary conditions, as well as eruption parameters compatible with the best CME candidate observed on this flare star.

The outline of this article is as follows. Models, boundary conditions, and numerical setup are presented in Section 2. The stellar wind steady-state solutions, time-dependent CME simulations, and the expected space environment for the exoplanets of the AU Mic system are presented and discussed in Section 3. We conclude and summarize our findings in Section 4.

2. Magnetically Driven Numerical Models

The simulations presented here are performed using the most recent version of the Space Weather Modeling Framework (SWMF; Gombosi et al. 2018).[9] This suite of physics-based models, originally developed for solar system science, allows a detailed numerical description of a wide range of spatial domains covering different objects of interest—from local simulations of convection to global models of planetary magnetospheres and the heliosphere (see Tóth et al. 2005, 2012). In recent years, models incorporated in the SWMF have been used by different authors to study the space environment of other late-type stars and their exoplanets (e.g., Garraffo et al. 2016; Nicholson et al. 2016; Vidotto & Donati 2017; Cohen et al. 2020).

To investigate the expected space weather surrounding AU Mic we consider two coupled models of the SWMF. These correspond to the Alfvén Wave Solar Model (AWSoM; van der Holst et al. 2014) and the Titov & Démoulin (1999) flux rope eruption model, both of which have been validated in multiple studies of the Sun–Earth environment (e.g., Jin et al. 2013; Sachdeva et al. 2019; van der Holst et al. 2019).

2.1. Corona and Stellar Wind Model

The dissipation of Alfvén waves in the upper chromosphere constitutes the main mechanism behind the coronal heating and the acceleration of the stellar wind within AWSoM. These contributions appear as additional source terms in the nonideal magnetohydrodynamic (MHD) momentum and energy relations, which are solved alongside the magnetic field induction and mass conservation equations. Electron heat conduction and radiative losses are also incorporated in the simulation.

As described by van der Holst et al. (2014), AWSoM-specific proportionality constants, together with the base plasma density ($n_0 = 2 \times 10^{10}$ cm^{-3}) and temperature ($T_0 = 5 \times 10^4$ K), are required as boundary conditions. For the models discussed here, we assume the same set of AWSoM parameters[10] as in the M-dwarf simulations presented in Alvarado-Gómez et al. (2020b), adjusting the basic stellar properties to AU Mic ($M_\bigstar = 0.5\ M_\odot$, $R_\bigstar = 0.75\ R_\odot$, $P_{\rm rot} = 4.85$ days; Kiraga 2012; Plavchan et al. 2020).

In order to calculate the required propagation and reflection of Alfvén waves, AWSoM also uses the distribution of the radial magnetic field ($B_{\rm R}$) on the stellar surface as input. For simulations in the stellar regime, this information can be retrieved from spectropolarimetric observations and Zeeman–Doppler Imaging (ZDI) magnetic field reconstructions (Donati & Brown 1997, Piskunov & Kochukhov 2002).

In the case of AU Mic, two recent observational studies have provided information on the properties of its large-scale magnetic field. Kochukhov & Reiners (2020) obtained the first ZDI map of this star, revealing a nonaxisymmetric field with a (signed) average strength of ∼88 G and values up to ∼184 G in local regions (Figure 1, Case 1). However, the authors caution that due to the particular line-of-sight orientation of AU Mic (close to 90° of inclination), ZDI reconstructions employing circular polarization alone would not be sensitive to components antisymmetric with respect to the stellar equator (e.g., a dipole aligned with the stellar rotation axis). To circumvent this limitation, Kochukhov & Reiners (2020) analyzed the Zeeman signatures from AU Mic in linear polarization, which indicates the presence of an additional axisymmetric large-scale dipole field of ∼2.0 kG (Figure 1, Case 2). Employing a different set of circular polarization observations, Klein et al. (2021) reported a second ZDI map of AU Mic. This map is characterized by a 450 G large-scale dipole field inclined by 19° with respect to the rotation axis, displaying an average longitudinal magnetic field strength of 475 G (Figure 1, Case 3). The effects from the equator-on orientation of AU Mic were not discussed by Klein et al. (2021) in their ZDI reconstruction. The radial magnetic field maps, incorporated at the inner boundary of our simulations, are presented in the different panels of Figure 1.

The grid in our simulations is spherical, with the inner boundary representing the stellar surface ($\sim 1\,R_\bigstar$), and the rotation axis of the star aligned with the z Cartesian direction.

---

[9] csem.engin.umich.edu/tools/swmf/

[10] Corresponding to the Alfvén wave correlation length $L_\perp \sqrt{B} = 1.5 \times 10^5$ m $\sqrt{\rm T}$ and the scaling of the Alfv́en wave Poynting flux $({\rm S/B})_\bigstar = 1.1 \times 10^6$ W m^{-2} T^{-1}.

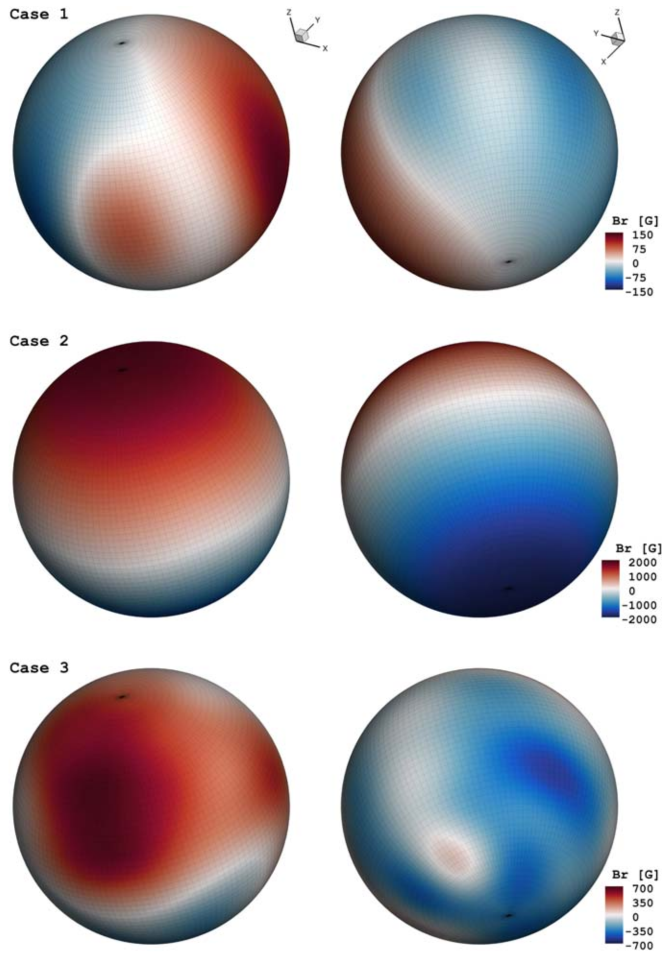

Figure 1. North (left) and south (right) poleward views of the three radial magnetic field configurations driving our corona/stellar wind models for AU Mic. Case 1 is provided by the nominal ZDI reconstruction obtained by Kochukhov & Reiners (2020), while Case 2 includes an extra 2 kG axisymmetric dipole (see text for details). Case 3 corresponds to the ZDI map reported by Klein et al. (2021). Note the different B_R ranges in each case.

The spatial resolution is higher at the surface ($\Delta R = 0.025\, R_\bigstar$, $\Delta\Phi = 1.4^{\circ}$[11]), with a radial stretching factor $\propto \ln(R)$. Given the varying maximum field strength of the input ZDI maps (see Figure 1), a different domain size is employed for each run: $80\, R_\bigstar$ (Case 1), $200\, R_\bigstar$ (Case 2), and $120\, R_\bigstar$ (Case 3). This is done to guarantee a closed Alfvén surface (AS) of the stellar wind, necessary for a correct description of the escaping wind solution within each three-dimensional domain. From an initial finite-difference potential field extrapolation (Tóth et al. 2011), the simulations evolve until a steady-state solution is reached.

2.2. Flux Rope CME Model

The SWMF implementation of the Titov & Démoulin (TD; 1999) flux rope eruption model is used to perform our CME simulations. This model is based on a prescribed magnetic tension imbalance between the ambient magnetic field configuration (provided by the AWSoM steady-state solution) and a twisted magnetic loop inserted at the inner boundary of the domain (see, e.g., Tóth et al. 2007). The initialization of the TD flux rope requires seven parameters describing its location (2), orientation, size (2), loaded mass (M^{FR}), and magnetic free energy available in the eruption ($E_{\mathrm{B}}^{\mathrm{FR}}$).

Table 1
Initialization Parameters of the TD Flux Rope CME Simulation on AU Mic

Parameter	Value	Unit
Tilt angle[a]	215.0	deg
Longitude	330.0	deg
Latitude	9.6	deg
Radius (R^{FR})	20.0	Mm
Length (L^{FR})	99.5	Mm
Mass (M^{FR})	10^{19}	g
Magnetic energy ($E_{\mathrm{B}}^{\mathrm{FR}}$)	4.2×10^{37}	erg

Note.
[a] Measured with respect to the stellar equator in the counterclockwise direction.

Table 1 contains the model parameters employed in our TD flux rope CME simulation on AU Mic. Both tilt angle and longitude were chosen in such a way that the inserted flux rope would lie in the vicinity of a polarity inversion line on all three surface-field configurations. For the anchoring latitude, we used one of the values of the starspot locations on AU Mic derived from the photometric light-curve modeling performed by Wisniewski et al. (2019). This selection was made so that the emerging CMEs would have a higher probability of impacting the planets lying in the equatorial plane of the system. The remaining parameters were adjusted so that the inserted TD flux rope would be able to power a CME with mass and kinetic energy consistent with the best candidate event observed in this star so far ($M^{\mathrm{CME}} \sim 10^{20}$ g, $E_{\mathrm{K}}^{\mathrm{CME}} \sim 10^{36}$ erg; Katsova et al. 1999).

After the TD flux rope insertion, the evolution of the resulting CME on each surface magnetic field configuration is followed by a time-dependent simulation covering 90 minutes (real-time), with full-domain snapshots extracted at a cadence of 1 minute. Note that while the spatial resolution in our simulations is not able to capture the internal structure of the flux rope (six resolution elements between the flux rope ends at the surface), it is sufficient to describe its global evolution and the subsequent CME propagation within the domain.

3. Results and Discussion

Below we present the results obtained for each of our ZDI-driven corona/stellar wind models of AU Mic. These are used to derive expected steady and transient conditions (due to an energetic CME event) around the star and to evaluate the space environment experienced by the exoplanets of this system.

3.1. Quiescent Stellar Wind Conditions around AU Mic

The three panels of Figure 2 contain the steady-state stellar wind solutions obtained for AU Mic, employing observed large-scale magnetic field distributions of this star as boundary conditions (Section 2). For each case we include the orbits of planets b and c (Section 1), as well as the AS of the stellar wind. This structure is defined by the spatial locations with an Alfvénic Mach number $M_{\mathrm{A}} = 1$, where the wind velocity matches the Alfvén speed V_{A} (i.e., $M_{\mathrm{A}} \equiv U/V_{\mathrm{A}} = U\sqrt{4\pi\rho}/B = 1$, where ρ, U, and B correspond to the local stellar wind density, velocity, and magnetic field strength, respectively).

---

[11] Here Φ denotes both angular directions in spherical coordinates (azimuthal and meridional).

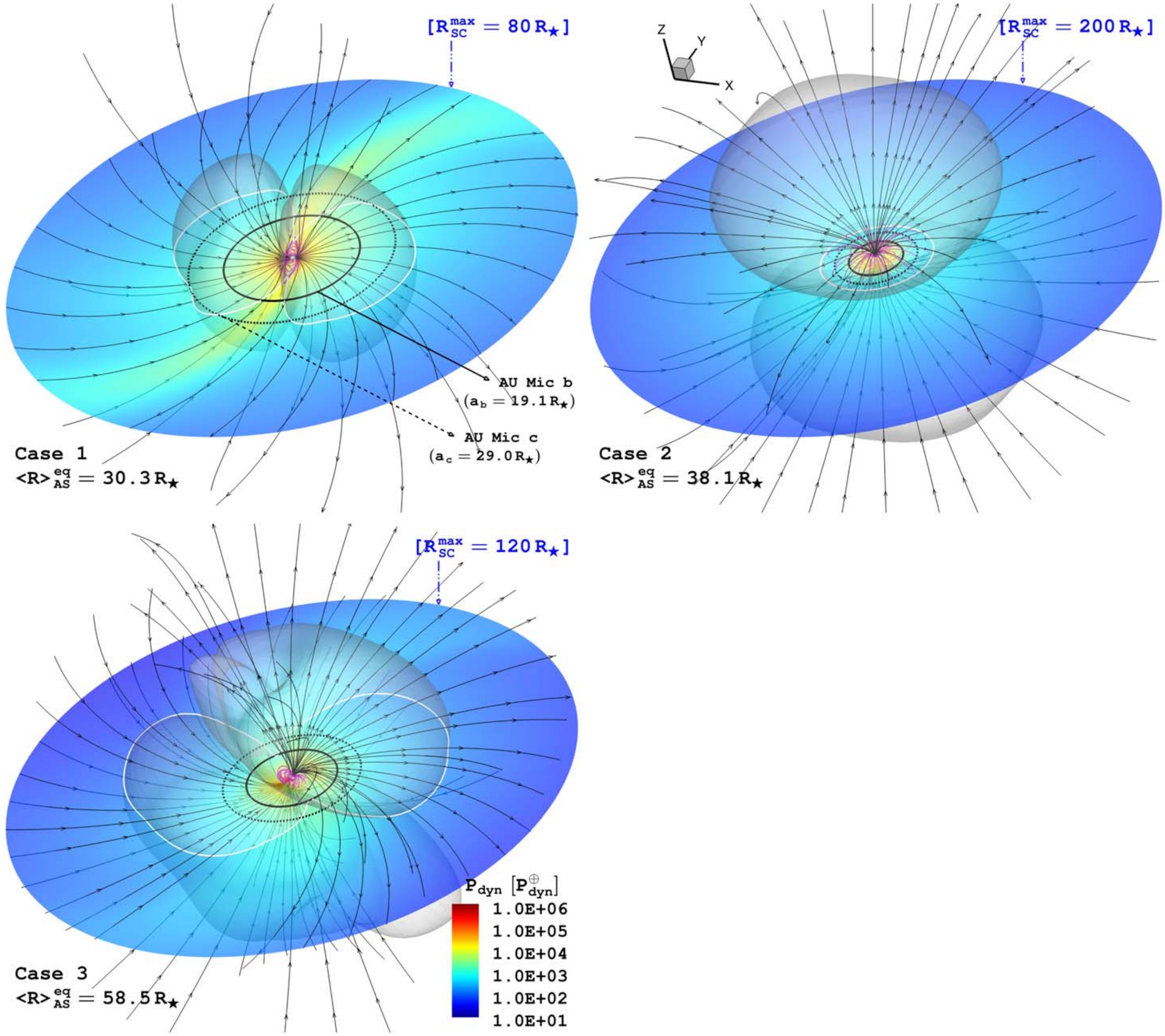

Figure 2. Simulated stellar wind environment for AU Mic driven by the different ZDI maps of the star (see Figure 1). A common color scale denotes the equatorial distribution of the stellar wind dynamic pressure ($P_{\rm dyn}$) normalized to the average Sun–Earth value ($P_{\rm dyn}^{\oplus} = 1.5$ nPa). Solid and dashed lines indicate the orbits of AU Mic b and c, respectively. A translucent shade shows the resulting Alfvén surface (AS) of the stellar wind in each case (see text for details). The equatorial projection of the AS (white solid line) and its average radius are indicated. Selected closed (magenta) and open (black with arrows) magnetic field lines are shown. The field of view on each panel has been adjusted to show the entire SC domain for the respective case.

The AS establishes the boundary for the escaping stellar wind ($M_{\rm A} > 1$) and the magnetically coupled outflows in the corona ($M_{\rm A} < 1$) that could still fall back to the star. The AS also separates the sub- and super-Alfvénic regimes of the stellar wind, which will influence dramatically the structure of any magnetosphere/ionosphere around an orbiting planet in the system (see Cohen et al. 2014 and references therein).

In line with other stellar wind studies (e.g., Cohen & Drake 2014; Vidotto et al. 2014; Réville et al. 2015), stronger surface magnetic fields lead to faster stellar winds and larger AS structures. The terminal radial wind speeds[12] within the respective simulation domains were roughly $1150\,{\rm km\,s^{-1}}$ (at $80\,R_\star$, Case 1), $2200\,{\rm km\,s^{-1}}$ (at $200\,R_\star$, Case 2), and $2000\,{\rm km\,s^{-1}}$ (at $150\,R_\star$, Case 3). Similarly, we obtain average AS radii of $27.8\,R_\star$ (Case 1), $106.4\,R_\star$ (Case 2), and $73.1\,R_\star$ (Case 3). In terms of the stellar wind mass-loss rates ($\dot{M}_\star$), our models yield values between ~5 and 10 $\dot{M}_\odot$.[13]

Unfortunately, there are no observational constraints on the stellar wind properties of AU Mic. Applying the observed coronal/disk properties in this system to the results of theoretical, numerical, and semiempirical studies from the literature (Augereau & Beust 2006; Strubbe & Chiang 2006;

---

[12] Taken as the maximum value achieved at the outer boundary of the simulation.

[13] Where $\dot{M}_\odot \simeq 2 \times 10^{-14}\,M_\odot\,{\rm yr^{-1}} = 1.265 \times 10^{12}\,{\rm g\,s^{-1}}$.

Cranmer et al. 2013; Schüppler et al. 2015) leads to mass-loss rate estimates $\dot{M}_\bigstar \sim 10$–$300\,\dot{M}_\odot$. Very recently, Kavanagh et al. (2021) simulated the stellar wind of AU Mic using the ZDI map of Klein et al. (2021) as a boundary condition (Case 3). They report solutions with low ($\dot{M}_\bigstar = 27\,\dot{M}_\odot$) and high ($\dot{M}_\bigstar = 590\,\dot{M}_\odot$) mass-loss rates.[14] It is good to note that our relatively low $\dot{M}_\bigstar$ values appear close to estimates from stellar wind astrospheric detections for other M-dwarf stars (Wood et al. 2021). Similarly, our resulting range of mass-loss rate per unit surface area on AU Mic ($\dot{M}_\bigstar / A_\bigstar = \dot{M}_\bigstar / 4\pi R_\bigstar^2 \simeq 9 - 18\,\dot{M}_\odot / A_\odot$) is consistent[15] with the Lyα astrospheric constraint available for EV Lac (M3.5V, $P_{\rm rot} = 4.38$ days, $F_{\rm X} = 1.56 \times 10^7$ erg cm^{-2} s^{-1}, $\dot{M}_\bigstar / A_\bigstar \simeq 9.8\,\dot{M}_\odot / A_\odot$; Wood et al. 2005), which displays very similar rotation and coronal activity to AU Mic ($P_{\rm rot} = 4.85$ days, $F_{\rm X} = 1.60 \times 10^7$ erg cm^{-2} s^{-1}).

Both transiting planets in the AU Mic system lie very close to the equatorial plane (i.e., $i \simeq 90°$; Martioli et al. 2021). Figure 2 shows the projection of the AS (white solid line) as well as its average size on this plane $\langle R \rangle_{\rm AS}^{\rm eq}$. In all three cases, we find that for the majority (if not the totality) of their orbit, both planets remain inside the sub-Alfvénic regime of the stellar wind. As described by Cohen et al. (2014), a planetary global magnetosphere within such a sub-Alfvénic stellar wind will tend to be open (similar to the Alfvén wing configuration observed in the Galilean moons; see Neubauer 1998). Under those conditions, the magnetic field of the star and the planet could reconnect directly, impeding the generation of a bow-shock structure (see Strugarek 2021). This could modify drastically the amount of stellar wind energy dissipated into the planetary ionosphere/atmosphere (Cohen et al. 2018), as well as the observable patterns of evaporative outflows from the exoplanets in the system (Harbach et al. 2021).

Note also that the 2 kG dipole aligned with the stellar rotation axis in Case 2 generates a *smaller* $\langle R \rangle_{\rm AS}^{\rm eq}$ compared to the 450 G inclined dipole from Case 3. This follows from a general result of magnetically driven stellar winds models in which, for simple large-scale magnetic field geometries (i.e., dipole, quadrupole), the largest AS lobes are found right above the regions with the strongest magnetic field, while the smallest portions of the AS will emerge in the vicinity of the polarity inversion lines of the surface field (Garraffo et al. 2015; Vidotto et al. 2015; Alvarado-Gómez et al. 2016). In this way, a stellar dipole field aligned with the z-axis (as in the Case 2 simulation) will have a polarity inversion line coincident with the equatorial plane so that the resulting stellar wind AS will be the smallest at latitude 0°. On the other hand, the $\sim 20°$ inclination of the large-scale dipole field in Case 3 is sufficient to make the large lobes of the AS cross the equatorial plane, making it much bigger at that particular latitude despite the weaker surface field. This example clearly illustrates that the magnetic field strength alone is insufficient to characterize the stellar wind environment of a planet-hosting star. It is also worth bearing in mind that the secular change of the surface magnetic field due to the growth and decay of active regions, and perhaps also to a magnetic cycle, can change the location of the current sheet and the shape of the AS.

The visualizations of Figure 2 also display the stellar wind dynamic pressure ($P_{\rm dyn} = \rho\, U^2$), normalized to typical conditions experienced by Earth[16] ($P_{\rm dyn}^{\oplus}$). Within the three considered cases, we find values of $P_{\rm dyn}$ along the orbit of AU Mic b ranging between $\sim$1150 and 13,300 $P_{\rm dyn}^{\oplus}$, going down to $\sim$450–6800 $P_{\rm dyn}^{\oplus}$ for AU Mic c. Similar conditions have been predicted for the habitable-zone planet Proxima b (Garraffo et al. 2016), as well as for the exoplanet candidate Proxima d (Alvarado-Gómez et al. 2020a). Still, we find that the planetary environment around AU Mic is much harsher than for Proxima Centauri. The reason for this is that the relatively strong large-scale surface magnetism of AU Mic leads to magnetic pressure values ($P_{\rm mag} = B^2/8\pi \propto 1/R^6$) greater than the associated $P_{\rm dyn}$ at the exoplanet orbits (which is not the case for Proxima b). At the distance of AU Mic b, we find that, on average, $P_{\rm mag}$ appears larger than $P_{\rm dyn}$ by factors of 1.4 (Case 1), 11.1 (Case 2), and 5.2 (Case 3). Likewise, along the orbit of AU Mic c, Cases 2 and 3 show average $P_{\rm mag}$ values greater than $P_{\rm dyn}$ by factors of 2.3 and 2.0, respectively. Only in the simulation with the weakest surface magnetic field (Case 1) does the average $P_{\rm dyn}$ dominate over $P_{\rm mag}$ at the distance of AU Mic c (by a factor of $\sim$2.7). The quiescent environment obtained for the AU Mic planets then appears more comparable to the extreme conditions expected for the planets of the TRAPPIST-1 system (Garraffo et al. 2017).

3.2. Simulated CME Events in the AU Mic System

The steady-state stellar wind solutions discussed in the previous section serve as the initial state for our time-dependent CME simulations. The latter are driven by a single erupting TD flux rope, initialized with the parameters provided in Section 2.2. As expected, while the properties of the inserted flux rope are identical, the varying magnetic/stellar wind conditions among the three cases lead to quite different CMEs.

We follow the procedure introduced by Alvarado-Gómez et al. (2019a, 2020b) to identify and characterize our simulated CME events. For each solution, we compute the 3D density contrast $n(t)/n^{\rm SS}$, with $n(t)$ and $n^{\rm SS}$ as the instantaneous and pre-CME (steady-state) particle density distributions, respectively. The escaping CME front is traced by the collection of points on the time-evolving isosurface $n(t)/n^{\rm SS} = 3.0$ with radial speeds greater than the local escape velocity.[17] As different sections of the CME face dissimilar coronal and stellar wind conditions, the front expansion is highly inhomogeneous. To estimate the instantaneous maximum radial speed of the CME as a whole ($U_{\rm R,T}^{\rm CME}$), we take the mean position among the 1% outermost grid points forming the escaping front and determine the relative variation of this average value between consecutive frames (1 minute cadence). The escaping CME front also serves as the limit of integration for a volume integral of the plasma density, allowing the determination of the total mass ($M_{\rm T}^{\rm CME}$) and kinetic energy ($E_{\rm K,T}^{\rm CME}$) of the eruption at each time step.

This analysis revealed that during their evolution, the emerging CME structures enclosed two separate regions where the density contrast increased by more than one order of magnitude (i.e., $n(t)/n^{\rm SS} > 10$). Figure 3 shows the CME

---

[14] Kavanagh et al. (2021) assumed a different set of initial AWSoM parameters compared to the models presented here.

[15] Lyα astrospheric constraints of $\dot{M}_\bigstar$ are expected to be accurate within a factor of 2 (Wood et al. 2005).

[16] Corresponding to $\sim$1.5 nPa associated with a solar wind particle densities of $n \simeq 4$–5 cm^{-3} and a velocity of $U \simeq 450$ km s^{-1}.

[17] Given by $v_{\rm esc} = \sqrt{2GM_\bigstar/H}$, where H is the front height above the stellar surface and G is the gravitational constant.

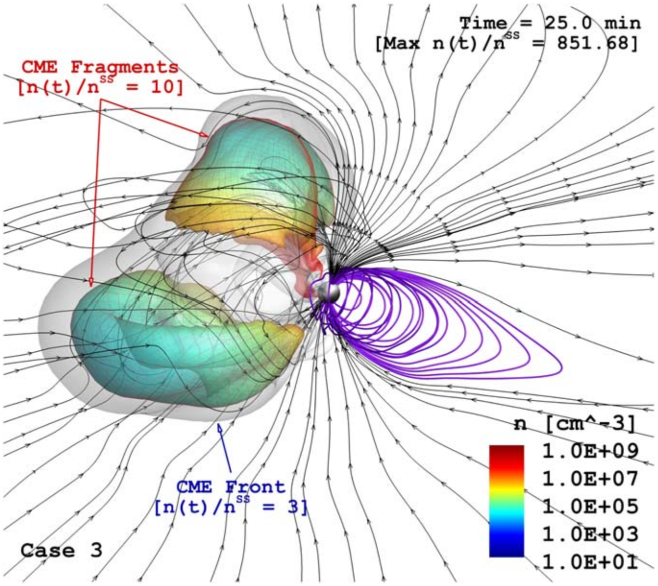

Figure 3. Example of the CME fragmentation that occurs in the Case 3 simulation. The instantaneous to steady-state density ratio, $n(t)/n^{\rm SS} = 3$, is used to identify the escaping CME structure (translucent isosurface) that envelops two spatially disconnected regions where the contrast in density is larger than one order of magnitude. The boundary of these CME fragments is taken as the $n(t)/n^{\rm SS} = 10$ isosurface, which is color-coded by the local plasma density (n) to emphasize their different properties and dynamics. Selected magnetic field lines in the far (purple) and erupting (black with arrows) sides are shown. The field of view of the visualization is 60 $R_\bigstar$.

fragmentation in Case 3, but it was also observed in the other runs as well. As can be seen in the visualization, despite having a launching latitude of only ∼10° (see Table 1), one of the CME fragments follows a high-latitude trajectory (close to the north pole of the star) whereas the second one propagates closer to the equator. Similar behavior was obtained on the strongest CME events analyzed in Alvarado-Gómez et al. (2018), where the large-scale stellar field only provided weak magnetic confinement. The Case 2 simulation, in which the large-scale dipole field is the strongest of all cases (see Figure 1), shows that the two CME fragments are slowly guided in opposite poleward directions. Interestingly, only in the simulation for Case 1, where the surface field lacks a large-scale dipole field (see Section 2.1), is the propagation of both CME fragments centered along the equatorial plane where the planets reside. These results are better illustrated in Figures 4 and 5, where the different snapshots correspond to the arrival time of the event at the orbit of AU Mic b (Figure 4) and AU Mic c (Figure 5).

To quantify parameters such as the speed ($U^{\rm CME}_{\rm R,1-2}$), mass ($M^{\rm CME}_{1-2}$), and kinetic energy ($E^{\rm CME}_{\rm K,1-2}$) of these CME fragments, we followed the methodology applied to the event as a whole, taking in this case an $n(t)/n^{\rm SS} = 10$ isosurface as the boundary of reference. Table 2 contains time averages of the CME properties for the entire event, as well as values associated with the individual CME fragments on each run. Notice that in all cases the global values of $\langle M^{\rm CME}_{\rm T}\rangle$ are close to two orders of magnitude lower than the CME candidate event parameters reported on AU Mic by Katsova et al. (1999) and roughly five times lower than the amount of mass originally inserted in the TD flux rope (see Table 1). This indicates that an important fraction of the flux rope eruption does not escape and remains magnetically confined in the low corona (see Alvarado-Gómez et al. 2019a). Despite this, the escaping eruptions display $\langle E^{\rm CME}_{\rm K,T}\rangle$ values consistent with the observed CME candidate event in this star.

In further agreement with the CME magnetic suppression results of Alvarado-Gómez et al. (2018), the mean total mass of the eruptions is comparable between Cases 1 and 2, while the presence of a strong surface large-scale magnetic field in the latter case leads to an important reduction in the CME radial speed (∼50%) and kinetic energy (∼65%). Interestingly, the Case 3 simulation (driven by a different geometry, which includes an inclined 450 G large-scale dipole field; see Section 2.1) only shows a minor reduction in $\langle U^{\rm CME}_{\rm R,T}\rangle$ compared to Case 1 (by ∼5%). While further investigation is required, this suggests that the large-scale dipole field inclination will strongly influence the dynamical properties of an emerging CME.

In terms of the CME fragmentation, our calculations indicate that at least one fragment propagates with a similar speed to the global CME, and that combined they carry a significant fraction of the total escaping CME mass (between 60% and 90%). However, the mass distribution among them is not uniform, with one fragment being considerably more massive than the other (see Table 2). For Cases 1 and 3, this mass discrepancy translates to a difference of more than one order of magnitude in the average kinetic energy of each CME fragment. The situation is more balanced in Case 2, as the lighter CME fragment compensates by traveling at a higher speed.

As can be seen from Figures 4 and 5, the impact of the CME on the exoplanets in the system will be mediated by the fragmentation of the eruption. Depending on the large-scale magnetic field geometry, both exoplanets can be strongly affected by one or two CME fragments (Cases 1 and 3) or can receive a relatively weak perturbation compared with the global energetics of the entire event (Case 2). In the following section, we evaluate how the space weather environment at the exoplanet orbits is affected by the arrival and passing of these CMEs.

3.3. Space Weather Forecast for AU Mic b and c

Figure 6 shows the conditions along the orbit of AU Mic b during the evolution of the exoplanet-effective CMEs emerging from each analyzed case. We include the behavior of local dynamic pressure ($P_{\rm dyn}$, left) as well as its ratio to the magnetic pressure ($P_{\rm dyn}/P_{\rm mag}$, right). An analogous diagram along the orbit of AU Mic c is presented in Figure 7. The steady-state solutions (Figure 2, Section 3.1) provide the conditions at $t = 0$ minutes in these time-phase representations.

Apart from differences in the CME speeds, the visualizations of Figures 6 and 7 reveal various noteworthy features. The CME arrival in all cases is characterized by an extremely sharp increase in $P_{\rm dyn}$ with respect to the pre-CME state —roughly of two to four orders of magnitude for planets b and c, respectively. While the CME conditions are harsher in absolute terms for the planet closer to the star, the milder steady-state stellar wind environment surrounding the outermost planet leads to a larger $P_{\rm dyn}$ jump at the CME arrival.

In the denser regions of the expanding CME front (forming the cores of the CME fragments reaching the planets;[18] see Figures 4 and 5), $P_{\rm dyn}$ rises to values up to 10^8 times the dynamic pressure experienced by Earth on nominal solar wind

---

[18] In the Case 1 simulation, the arrival of the second CME fragment at the orbit of AU Mic b can be seen around $t \simeq 70$ minutes (Figure 6, top-left panel).

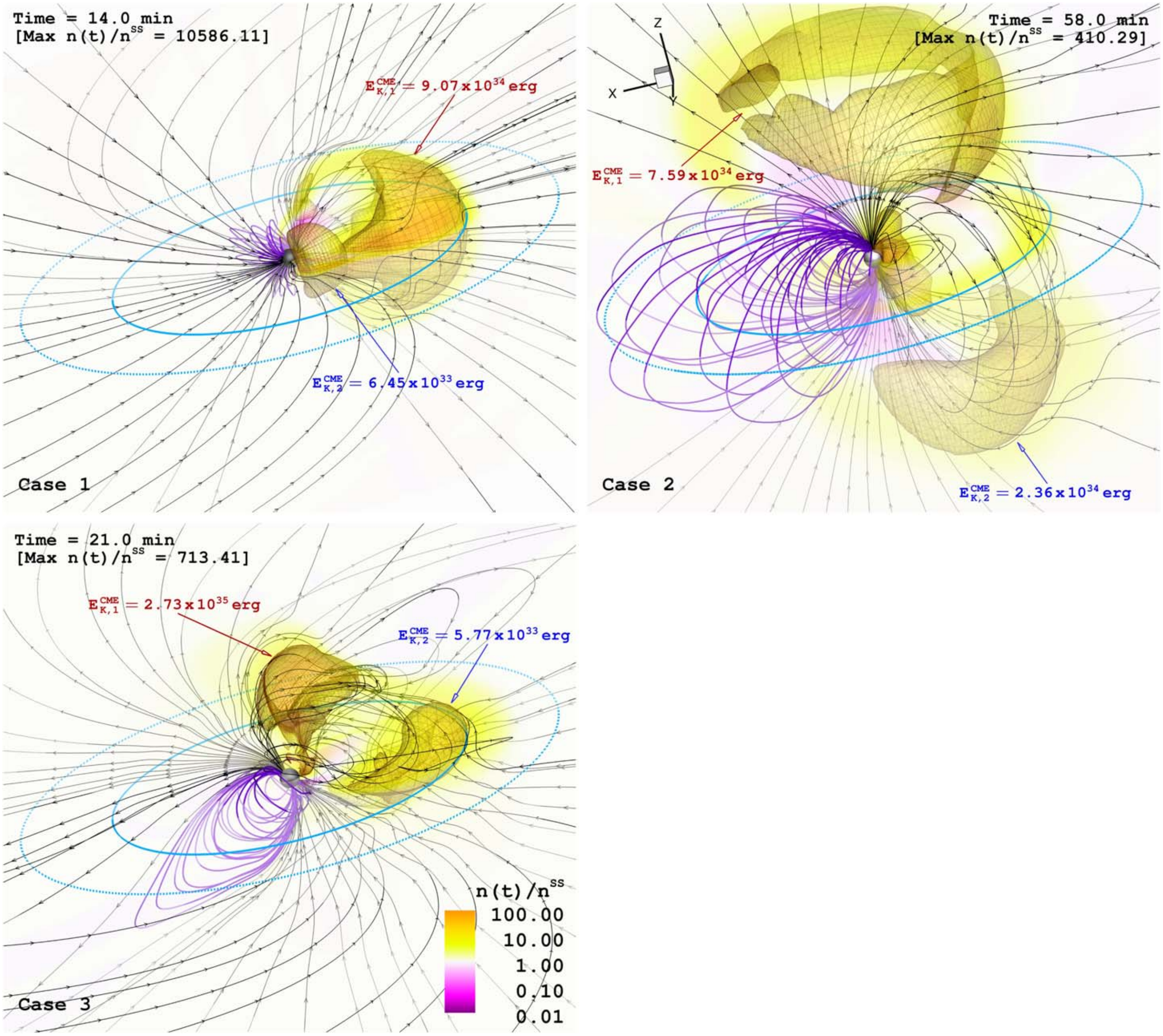

Figure 4. Results of the CME simulations in the AU Mic system. The panels contain the emerging CMEs for each considered magnetic field/stellar wind case (Sections 2 and 3.1). The color scale denotes the time-dependent density contrast $n(t)/n^{\rm SS}$, with the $n(t)/n^{\rm SS} = 10$ isosurface identifying the individual CME fragments. The snapshots show the perturbation arrival time at the orbit of AU Mic b (solid cyan line), with the instantaneous kinetic energy of each CME fraction indicated ($E_{\rm K,1-2}^{\rm CME}$). Note that for Case 2 (top right) the main fragments travel toward the polar regions and only a weaker perturbation arrives at the planet's orbits. Selected magnetic field lines in the far (purple) and erupting (black with arrows) sides are shown. The field of view is 60 $R_\bigstar$. An animation of this figure is available. The animation shows rotation of the 3D domain with a real-time duration of 6 seconds.

(An animation of this figure is available.)

conditions. Even the arrival of a Carrington-type CME event at Earth's orbit would induce a $P_{\rm dyn}$ transient five orders of magnitude smaller.[19] While such $P_{\rm dyn}$ values also exceed by far the total pressure ($P_{\rm dyn} + P_{\rm mag}$) predicted for planets orbiting low-mass stars at much closer distances compared to the AU Mic planets (e.g., Vidotto et al. 2015; Garraffo et al. 2017), these extreme CME-driven conditions persist only for a relatively short time (tens of minutes for the events considered here). Therefore, their global impact on a given atmospheric and magnetospheric structure of an exoplanet will mainly depend on the effective escaping CME rate of the star (mediated by the stellar large-scale magnetic field).

The bulk of the eruption strongly affects a large fraction of the orbit of both exoplanets—between 60% and 100% depending on the case. In those regions the dynamic pressure ranges from $10^6\, P_{\rm dyn}^{\oplus}$ down to a few $10^4\, P_{\rm dyn}^{\oplus}$. As illustrated in the right panels of Figures 6 and 7, these values are sufficient to overcome the general dominance of $P_{\rm mag}$ in this system. Furthermore, the CME-driven enhancement in the local plasma density and velocity will shift the conditions along the affected orbital phases from the sub-Alfvénic to the super-Alfvénic

---

[19] Assuming a density contrast of $n(t)/n^{\rm SS} = 20$ and a CME speed of 3000 km s^{-1} (see Baker et al. 2013).

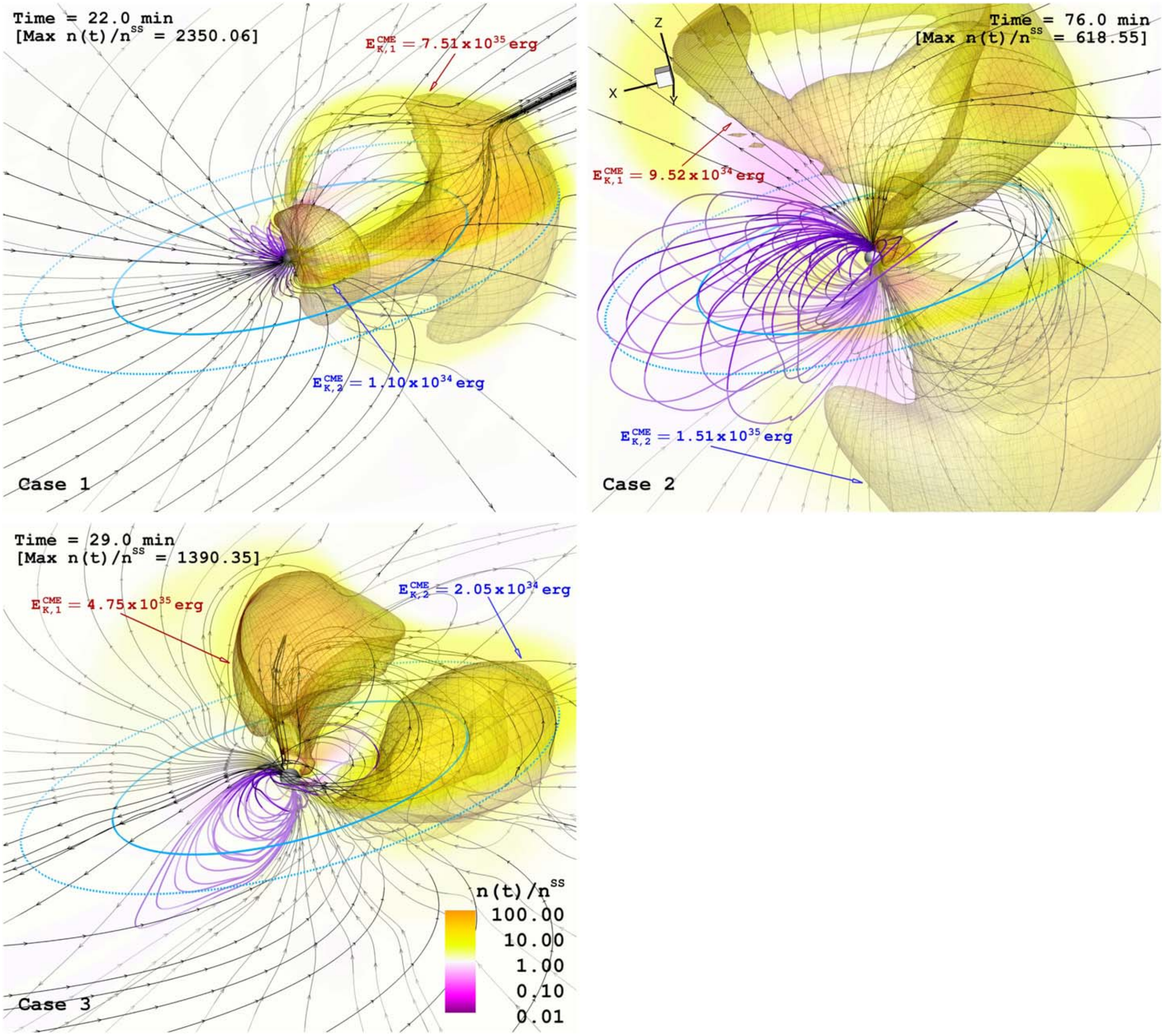

Figure 5. Results of the CME simulations in the AU Mic system. See caption of Figure 4. The snapshots correspond to the perturbation arrival time at the orbit of AU Mic c (dashed cyan line), with the instantaneous kinetic energy of each CME fraction indicated ($E^{\rm CME}_{\rm K,1-2}$). An animation of this figure is available. The animation shows rotation of the 3D domain with a real-time duration of 6 seconds.

(An animation of this figure is available.)

Table 2
Properties Obtained in the Simulated CME Events on AU Mic

Case	# of CME Fragments[a]	$\langle M^{\rm CME}_{\rm T}\rangle$ (10^{18} g)	$\langle U^{\rm CME}_{\rm R,T}\rangle$ (km s^{-1})	$\langle E^{\rm CME}_{\rm K,T}\rangle$ (10^{35} erg)	$\langle M^{\rm CME}_{1}\rangle$ (10^{18} g)	$\langle U^{\rm CME}_{\rm R,1}\rangle$ (km s^{-1})	$\langle E^{\rm CME}_{\rm K,1}\rangle$ (10^{35} erg)	$\langle M^{\rm CME}_{2}\rangle$ (10^{18} g)	$\langle U^{\rm CME}_{\rm R,2}\rangle$ (km s^{-1})	$\langle E^{\rm CME}_{\rm K,2}\rangle$ (10^{35} erg)
1	2	2.15	10146	9.45	1.46	9924	6.24	0.56	4112	0.41
2	2	1.94	5102	3.51	0.95	4078	0.73	0.27	4968	0.65
3	2	2.51	9653	12.8	2.19	8278	8.53	0.09	9631	0.39

Notes. Parameters for the events as a whole (T) as well as for the individual CME fragments (1, 2) are included (see text for details). Values listed in columns 3–11 correspond to temporal averages of instantaneous maxima during the entire event evolution.

[a] Identified by spatially disconnected escaping perturbations with $n(t)/n^{\rm SS} \geqslant 10$.

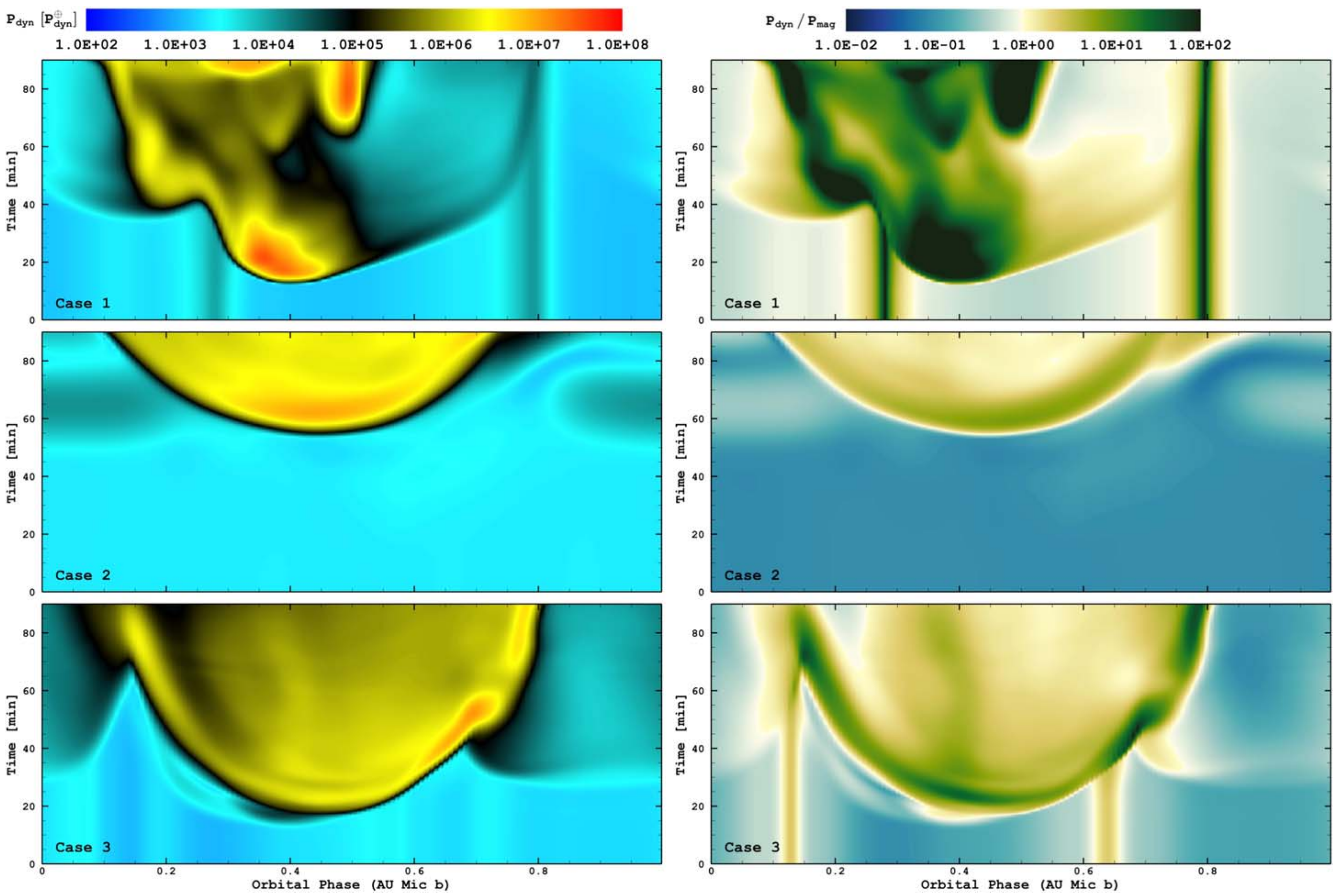

Figure 6. Temporal evolution of the space weather conditions along the orbit of AU Mic b during the simulated CME events (Section 3.2). The behavior of $P_{\rm dyn}$ (left) and $P_{\rm dyn}/P_{\rm mag}$ (right) is shown for each considered case as indicated (see Figure 4). The values of $P_{\rm dyn}$ are normalized to the typical conditions experienced by Earth ($P_{\rm dyn}^{\oplus} = 1.5$ nPa). The vertical features in Cases 1 (phases 0.25 and 0.78) and 3 (phases 0.10 and 0.63) correspond to the high-density stellar wind streamers associated with the current sheet.

regime (see Section 3.1). However, this situation is expected to be temporary, as the sub-Alfvénic conditions along the orbit return once the stellar wind has relaxed into a new steady state (not captured in our simulations).

One interesting and counterintuitive consequence of this CME-driven transition is that the eruption passage would shut down any possible planet-induced stellar radio emission via electron cyclotron maser instability (ECMI; see Saur et al. 2013; Kavanagh et al. 2021). This type of emission is expected to occur in star–planet interactions (SPIs) within the sub-Alfvénic regime of the stellar wind, where Alfvén waves traveling toward the star would carry enough energy to induce radio emission via ECMI in the stellar corona (Turnpenney et al. 2018). As the sub-Alfvénic regime is temporarily lifted by the CME passage, the dimming of this radio signal (assuming that a pre-CME baseline could be detected and isolated from other possible stellar sources) may potentially serve to find candidate CME events on the host star—analogous to coronal dimming events observed in the Sun and other stars (see Mason et al. 2016; Veronig et al. 2021). Furthermore, if such a CME event would be associated with a flare, the radio-dimming time lag should be able to yield an estimate of the CME speed (provided that the orbit of the exoplanet is known). While their characterization is beyond the scope of this paper, these SPI-ECMI radio-dimming features could constitute an alternative pathway to study the eruptive behavior of exoplanet hosts. This is not only relevant as the information on stellar CMEs in general is very scarce (see Argiroffi et al. 2019; Moschou et al. 2019) but also because the radio properties of cool stars at low frequencies are starting to be unveiled using ground-based observations (Vedantham et al. 2020; Callingham et al. 2021).

Finally, as noted in Section 1, observations have shown considerable flare activity in AU Mic, with estimated rates in the range of 5.54–6.35 flares/day for events with bolometric energies $E^{\rm FL} < 10^{32}$ erg, down to one event every 10 days for large flares with $E^{\rm FL} \sim 10^{34}$ erg (Martioli et al. 2021; Gilbert et al. 2022). As such, on a given rotation AU Mic displays on the order of 25–30 flaring events with $E^{\rm FL} < 10^{32}$ erg and about 5 flares that reach 10^{33} erg in bolometric energy. Even though CMEs associated with this flare activity will suffer strong magnetic suppression, a quiescent state in AU Mic (described in Section 2.1 and also by other authors in previous studies) might not represent the most common conditions around this flare star and its exoplanets. Such conditions are expected to be characterized by a rapidly changing corona and stellar wind environment, with considerable variability on a subrotational period timescale.

While the flare-CME candidate inspiring our simulations will not be as frequent as those milder events,[20] its evolution

---

[20] Extrapolating the flare frequency distribution from Gilbert et al. (2022) to the estimated energy of the event ($E^{\rm FL} > 10^{35}$ erg, Katsova et al. 1999) yields a cumulative rate <1 flare/100 days.

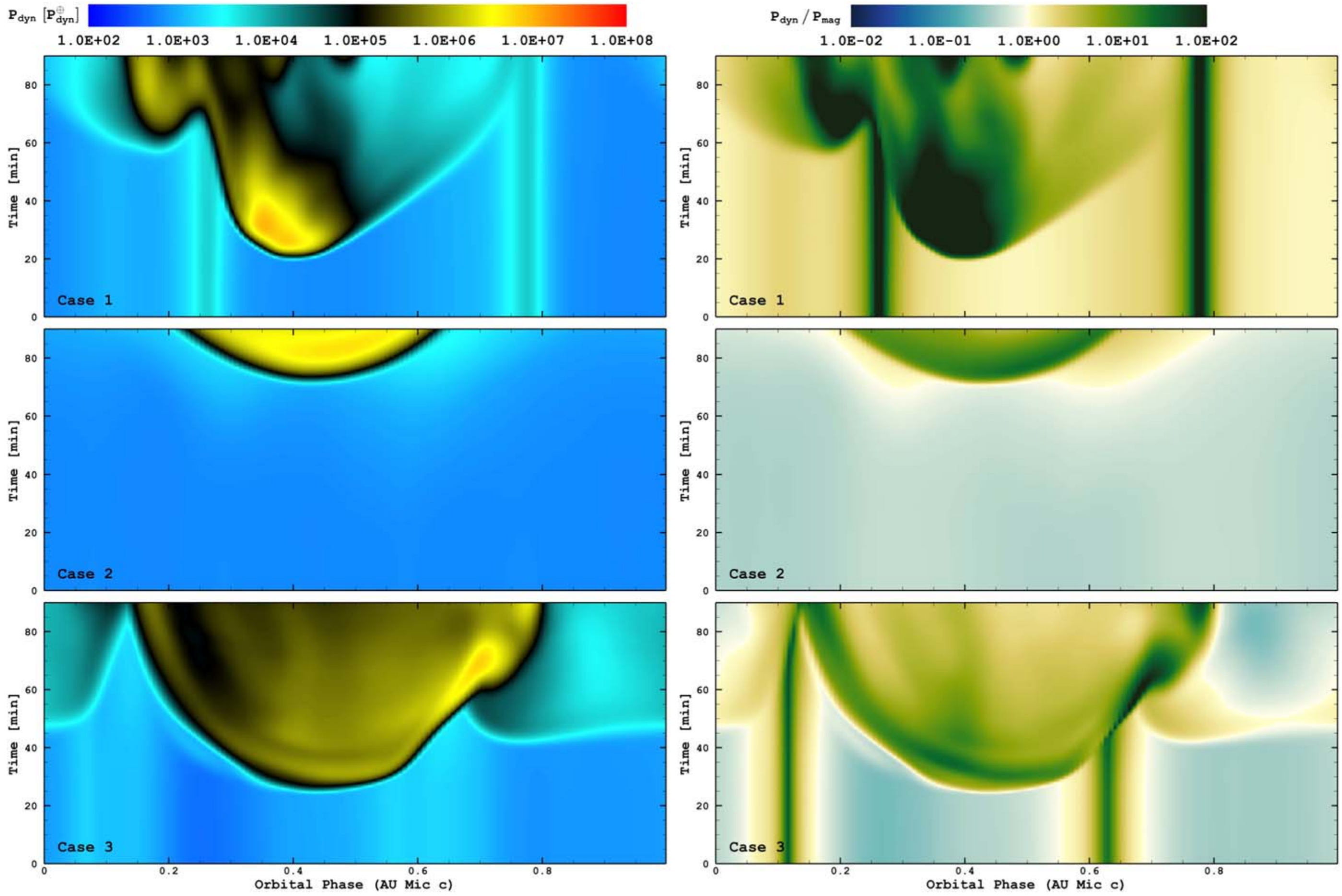

Figure 7. Temporal evolution of the space weather conditions along the orbit of AU Mic c during the simulated CME events. See caption of Figure 6.

reveals how much the space weather of the exoplanets and the entire inner astrosphere can be affected by these energetic transients. The resulting CME fragmentation leads to a wide range of latitudes, including the polar regions, being disturbed by the expanding structures (Figures 4 and 5). Changes in the geometry of the AS as well as the complete disruption of the current sheet (see Figures 6 and 7) are just two examples of the CME influence on the circumstellar environment. As the typical timescale involved in all of these CME-related affectations is comparable to the exoplanets' transit times (3.56 hr for AU Mic b and 4.42 hr AU Mic c, Gilbert et al. 2022), any observational and/or modeling efforts performed on this object should include time-dependent effects in their analysis. We will pursue this research direction in two complementary numerical studies on AU Mic, evaluating the influence of this extreme CME on atmospheric outflow patterns from the innermost planet (O. Cohen et al. 2022, in preparation), as well as investigating the pre- and post-CME energetic particle environments in this system (F. Fraschetti et al. 2022, in preparation).

4. Summary and Conclusions

In this study, we employed state-of-the-art numerical models to simulate the space weather of the planet-hosting flare star AU Mic. Two coupled models are used to characterize the quiescent stellar wind and the temporal evolution of a very energetic CME event in this system. Three different configurations of the large-scale magnetic field of AU Mic (inspired by Zeeman–Doppler Imaging observations), as well as eruption parameters sufficient to power the best CME candidate in this star, were incorporated as boundary conditions in our simulations.

The analyses of the steady-state and transient stellar wind conditions around the star were performed separately. Using the former, we showed that our models predict mass-loss rates in line with previous theoretical and numerical model expectations for AU Mic and with current observational constraints for other M dwarfs, including a measurement available for the flare star EV Lac (relatively similar to AU Mic in spectral type, rotation period, and activity levels).

Our results indicate that the planets of the AU Mic system experience extreme space weather conditions. In agreement with previous studies, we found that both exoplanets lie inside the sub-Alfvénic region of the stellar wind for the large majority of their orbits. At their respective orbital separations, AU Mic b and AU Mic c endure stellar wind dynamic pressures between two and four orders of magnitude larger than the average value experienced by Earth due to the solar wind. However, the conditions surrounding the AU Mic planets are most likely dominated by the local magnetic pressure, which can surpass the dynamic pressure of the stellar wind by relatively large factors (around 5–10 for some of the cases considered here).

For our modeling of the extreme CME event, a time-dependent simulation (initialized from each of the three ZDI-driven steady-state solutions) followed the evolution of an erupting twisted magnetic flux rope, which was anchored at the inner boundary of the domain. We found that, despite having identical parameters, the flux rope eruption generated different CMEs in terms of geometry, mass, velocity, and kinetic energy in the different starting wind solutions. These differences are attributed to the properties of the large-scale magnetic field (strength and topology), which also dictate the structure of the stellar wind in which the CMEs develop. In particular, the varying levels of magnetic suppression resulted in CMEs with global radial speeds between 5000 and 10,000 km s^{-1}, masses close to 2×10^{18} g, and kinetic energies within the 10^{35}–10^{36} erg range.

One common feature among all the simulated events was the fragmentation of the CME due to the confining influence of the large-scale field. Two main fragments emerged in each of our CME simulations, whose properties were isolated and compared with the behavior of the CME events as a whole. This analysis revealed that the redistribution of the total CME mass and kinetic energy among the fragments is not uniform, resulting in differences of more than one order of magnitude for these parameters. Additionally, while the launching location of the flux rope was near the stellar equator, the fragmentation of the eruption led to poleward CMEs in two out of the three cases considered. While further investigation is required, this situation might be connected with the presence of a “guiding” antisymmetric component in the large-scale magnetic field (absent in the case lacking these high-latitude CMEs).

Our simulations showed that CME fragmentation also plays a major role in determining the impact of the eruption on the AU Mic exoplanets. In the two cases displaying poleward CMEs, the perturbations arriving at the exoplanet orbits (aligned with the equatorial plane) were significantly less energetic compared with their high-latitude counterparts (differences in the CME kinetic energy of up to two orders of magnitude). From a purely CME dynamics point of view, if an antisymmetric large-scale magnetic field indeed enables a poleward fragmentation of the eruption, such magnetic topology could be beneficial for close-in exoplanets orbiting active stars. One particular case of such an antisymmetric field would be a large-scale dipole aligned with the stellar rotation axis. This configuration would have the additional benefit of a smaller stellar wind Alfvén surface at the equatorial plane, allowing super-Alfvénic orbits closer to the star with the possibility of closed magnetospheres around the planets (not possible for sub-Alfvénic orbits).

Finally, we also analyzed the effects along the exoplanet orbits due to the arrival of the exoplanet-effective CME fractions (traveling close to the equatorial plane). In all the considered cases, these eruptions completely altered the space weather conditions for large portions of the exoplanet orbit (between 60% and 100%). Their impact yielded dynamical pressure increases of between four to six orders of magnitude with respect to the steady state, with the largest increase being associated with the high-density CME fragment cores. The CME-induced dynamic pressure transient surpassed the local magnetic tension by large factors (between 10 and $>10^2$), temporarily shifting the exoplanetary conditions from sub-Alfvénic to super-Alfvénic. We briefly explored one possible implication of this transition, where the CME arrival at the exoplanet orbit would induce a radio-dimming event in the ECMI emission from SPIs. This feature, observable in principle using ground-based instrumentation, could open a window for future exploration of the still-elusive CME behavior in other stars.

J.J.D. and C.G. were funded by NASA contract NAS8-03060 to the CXC and thank the director, Patrick Slane, for continuing advice and support. O.C. was supported by NASA NExSS grant NNX15AE05G. F.F. was supported, in part, by NASA under grants NNX16AC11G and Chandra Theory Award Number $TM0-21001X$, $TM6-17001A$ issued by the Chandra X-ray Observatory Center, which is operated by the Smithsonian Astrophysical Observatory for and on behalf of NASA under contract NAS8-03060. K.P. and J.C. acknowledge funding from the German Leibniz Gemeinschaft under project number P67-2018. L.M.H. has received funding from the European Research Council (ERC) under the European Unions Horizon 2020 research and innovation program (grant agreement No. 853022, PEVAP). This work used SWMF/BATSRUS tools developed at The University of Michigan Center for Space Environment Modeling.

Software: SWMF (Gombosi et al. 2018).

ORCID iDs

Julián D. Alvarado-Gómez https://orcid.org/0000-0001-5052-3473
Ofer Cohen https://orcid.org/0000-0003-3721-0215
Jeremy J. Drake https://orcid.org/0000-0002-0210-2276
Federico Fraschetti https://orcid.org/0000-0002-5456-4771
Katja Poppenhaeger https://orcid.org/0000-0003-1231-2194
Cecilia Garraffo https://orcid.org/0000-0002-8791-6286
Judy Chebly https://orcid.org/0000-0003-0695-6487
Ekaterina Ilin https://orcid.org/0000-0002-6299-7542
Laura Harbach https://orcid.org/0000-0001-7944-0292
Oleg Kochukhov https://orcid.org/0000-0003-3061-4591

References

Alvarado-Gómez, J. D., Drake, J. J., Cohen, O., Moschou, S. P., & Garraffo, C. 2018, ApJ, 862, 93
Alvarado-Gómez, J. D., Drake, J. J., Fraschetti, F., et al. 2020b, ApJ, 895, 47
Alvarado-Gómez, J. D., Drake, J. J., Garraffo, C., et al. 2020a, ApJL, 902, L9
Alvarado-Gómez, J. D., Drake, J. J., Moschou, S. P., et al. 2019a, ApJL, 884, L13
Alvarado-Gómez, J. D., Garraffo, C., Drake, J. J., et al. 2019b, ApJL, 875, L12
Alvarado-Gómez, J. D., Hussain, G. A. J., Cohen, O., et al. 2016, AA, 594, A95
Argiroffi, C., Reale, F., Drake, J. J., et al. 2019, NatAs, 3, 742
Augereau, J. C., & Beust, H. 2006, A&A, 455, 987
Baker, D. N., Li, X., Pulkkinen, A., et al. 2013, SpWea, 11, 585
Boccaletti, A., Sezestre, E., Lagrange, A. M., et al. 2018, A&A, 614, A52
Boccaletti, A., Thalmann, C., Lagrange, A.-M., et al. 2015, Natur, 526, 230
Callingham, J. R., Vedantham, H. K., Shimwell, T. W., et al. 2021, NatAs, 5, 1233
Cohen, O., & Drake, J. J. 2014, ApJ, 783, 55
Cohen, O., Drake, J. J., Glocer, A., et al. 2014, ApJ, 790, 57
Cohen, O., Garraffo, C., Moschou, S.-P., et al. 2020, ApJ, 897, 101
Cohen, O., Glocer, A., Garraffo, C., Drake, J. J., & Bell, J. M. 2018, ApJL, 856, L11
Cranmer, S. R., Wilner, D. J., & MacGregor, M. A. 2013, ApJ, 772, 149
Cully, S. L., Fisher, G. H., Abbott, M. J., & Siegmund, O. H. W. 1994, ApJ, 435, 449
Donati, J.-F., & Brown, S. F. 1997, A&A, 326, 1135
Drake, J., Alvarado-Gómez, J. D., Airapetian, V., et al. 2019, BAAS, 51, 113
Fulton, B. J., Petigura, E. A., Howard, A. W., et al. 2017, AJ, 154, 109

Gaia Collaboration, Brown, A. G. A., & Vallenari, A. 2018, A&A, 616, A1
Garraffo, C., Drake, J. J., & Cohen, O. 2015, ApJL, 807, L6
Garraffo, C., Drake, J. J., & Cohen, O. 2016, ApJL, 833, L4
Garraffo, C., Drake, J. J., Cohen, O., Alvarado-Gómez, J. D., & Moschou, S. P. 2017, ApJL, 843, L33
Gilbert, E. A., Barclay, T., Quintana, E. V., et al. 2022, AJ, 163, 147
Gombosi, T. I., van der Holst, B., Manchester, W. B., & Sokolov, I. V. 2018, LRSP, 15, 4
Grady, C. A., Wisniewski, J. P., Schneider, G., et al. 2020, ApJL, 889, L21
Gronoff, G., Arras, P., Baraka, S., et al. 2020, JGRA, 125, e27639
Harbach, L. M., Moschou, S. P., Garraffo, C., et al. 2021, ApJ, 913, 130
Hünsch, M., Schmitt, J. H. M. M., Sterzik, M. F., & Voges, W. 1999, A&AS, 135, 319
Ibañez Bustos, R. V., Buccino, A. P., Flores, M., et al. 2019, MNRAS, 483, 1159
Jin, M., Manchester, W. B., van der Holst, B., et al. 2013, ApJ, 773, 50
Kalas, P., Liu, M. C., & Matthews, B. C. 2004, Sci, 303, 1990
Katsova, M. M., Drake, J. J., & Livshits, M. A. 1999, ApJ, 510, 986
Kavanagh, R. D., Vidotto, A. A., Klein, B., et al. 2021, MNRAS, 504, 1511
Kiraga, M. 2012, AcA, 62, 67
Klein, B., Donati, J.-F., Moutou, C., et al. 2021, MNRAS, 502, 188
Kochukhov, O., & Reiners, A. 2020, ApJ, 902, 43
Lépine, S., & Gaidos, E. 2011, AJ, 142, 138
MacGregor, A. M., Osten, R. A., & Hughes, A. M. 2020, ApJ, 891, 80
Magee, H. R. M., Güdel, M., Audard, M., & Mewe, R. 2003, AdSpR, 32, 1149
Martioli, E., Hébrard, G., Correia, A. C. M., Laskar, J., & Lecavelier des Etangs, A. 2021, A&A, 649, A177
Mason, J. P., Woods, T. N., Webb, D. F., et al. 2016, ApJ, 830, 20
Mitra-Kraev, U., Harra, L. K., Güdel, M., et al. 2005, A&A, 431, 679
Moschou, S.-P., Drake, J. J., Cohen, O., et al. 2019, ApJ, 877, 105
Neubauer, F. M. 1998, JGR, 103, 19843
Nicholson, B. A., Vidotto, A. A., Mengel, M., et al. 2016, MNRAS, 459, 1907
Owen, J. E. 2019, AREPS, 47, 67
Owen, J. E., & Wu, Y. 2013, ApJ, 775, 105
Owen, J. E., & Wu, Y. 2017, ApJ, 847, 29
Piskunov, N., & Kochukhov, O. 2002, A&A, 381, 736
Plavchan, P., Barclay, T., Gagné, J., et al. 2020, Natur, 582, 497
Redfield, S., Linsky, J. L., Ake, T. B., et al. 2002, ApJ, 581, 626
Réville, V., Brun, A. S., Matt, S. P., Strugarek, A., & Pinto, R. F. 2015, ApJ, 798, 116
Sachdeva, N., van der Holst, B., Manchester, W. B., et al. 2019, ApJ, 887, 83
Saur, J., Grambusch, T., Duling, S., Neubauer, F. M., & Simon, S. 2013, A&A, 552, A119
Schüppler, C., Löhne, T., Krivov, A. V., et al. 2015, A&A, 581, A97
Strubbe, L. E., & Chiang, E. I. 2006, ApJ, 648, 652
Strugarek, A. 2021, arXiv:2104.05968
Titov, V. S., & Démoulin, P. 1999, A&A, 351, 707
Tóth, G., de Zeeuw, D. L., Gombosi, T. I., et al. 2007, SpWea, 5, 06003
Tóth, G., Sokolov, I. V., Gombosi, T. I., et al. 2005, JGRA, 110, A12226
Tóth, G., van der Holst, B., & Huang, Z. 2011, ApJ, 732, 102
Tóth, G., van der Holst, B., Sokolov, I. V., et al. 2012, JCoPh, 231, 870
Turnpenney, S., Nichols, J. D., Wynn, G. A., & Burleigh, M. R. 2018, ApJ, 854, 72
van der Holst, B., Manchester, W. B., I., Klein, K. G., & Kasper, J. C. 2019, ApJL, 872, L18
van der Holst, B., Sokolov, I. V., Meng, X., et al. 2014, ApJ, 782, 81
Vedantham, H. K., Callingham, J. R., Shimwell, T. W., et al. 2020, NatAs, 4, 577
Veronig, A. M., Odert, P., Leitzinger, M., et al. 2021, NatAs, 5, 697
Vidotto, A. A., & Donati, J. F. 2017, A&A, 602, A39
Vidotto, A. A., Fares, R., Jardine, M., Moutou, C., & Donati, J.-F. 2015, MNRAS, 449, 4117
Vidotto, A. A., Gregory, S. G., Jardine, M., et al. 2014, MNRAS, 441, 2361
Wisniewski, J. P., Kowalski, A. F., Davenport, J. R. A., et al. 2019, ApJL, 883, L8
Wood, B. E., Müller, H.-R., Redfield, S., et al. 2021, ApJ, 915, 37
Wood, B. E., Müller, H.-R., Zank, G. P., Linsky, J. L., & Redfield, S. 2005, ApJL, 628, L143